scientific reports

Check for updates

OPEN

Tracing the relationship between the upper plate earthquake cycle and megathrust slip, the Atacama fault system in Northern Chile

Gabriel Gonzalez[1]✉, Luis Astudillo-Sotomayor[1,4], Ian Del Rio[2], André Oliveira Sawakuchi[2] & Will Amidon[3]

Inland-normal faulting is recognised as an important process following large subduction earthquakes. The lack of data limits the understanding of how normal fault reactivation relates to the subduction earthquake cycle. We characterised the palaeoseismology of the Atacama fault system (AFS) in the Chilean subduction zone. Our results showed that upper plate normal faulting earthquakes with M_w 7.0 and recurrence intervals of 35 ± 9 ky generated surface ruptures preserved as fault scarps. The average fault slip rate of 0.07 ± 0.01 m/kyr is three orders of magnitude slower than the convergence velocity, and the recurrence intervals of surface-rupturing earthquakes on the studied faults are much larger than the recurrence of great to giant (M_w > 8.5) subduction earthquakes in the Chilean margin. This demonstrates that the reactivation of an individual fault in the AFS is not always synchronised with this type of subduction earthquake.

Keywords Palaeoseismology, Upper plate fault, Chilean subduction, Atacama fault system, Luminescence dating, Seismic hazard

The 2010 Maule and 2011 Tohoku-Oki earthquakes triggered massive aftershocks in the forearc, illuminating the reactivation of dormant crustal faults[1–3]. Coseismic and postseismic relaxation produced rapid stress changes that brought the upper plate faults into the failure domain. Despite this observation, there is a substantial gap in understanding the temporal relationship between the recurrence time of large upper plate earthquakes and great subduction earthquakes. Two contributions[1,3] have demonstrated that the reactivation of the Itozawa Fault following the Tohoku-Oki earthquake have recurrence interval of coseismic rupture exceeding one magnitude order the elapsed time since the A.D. 869 Jogan earthquake, the penultimate great subduction earthquake in the Tohoku-Oki area[1]. This indicates that great earthquakes along the northeastern Japan trench do not always trigger the reactivation of normal faults. Similar conclusion has been derived in the subduction zone of central Chile, where the recurrence time of the reactivated Pichilemu Fault exceeds the recurrence time of the great subduction earthquakes in this part of the Chilean Margin[4]. Thus, recovering palaeoseismic data in upper plate faults is essential to fully grasp the complexities of this fault interaction.

In northern Chile, Quaternary normal faults rupturing at the topographic surface occur in the overriding plate[5], including the recognised Atacama fault system[6] (AFS, Fig. 1). These normal faults could represent primary examples of upper plate faults reactivated by great subduction earthquakes. Although the presence fault scarps along the AFS indicates the nucleation of earthquakes[7], there is no historical or instrumental record of seismic activity along this fault system. In the AFS, a previous work used optically stimulated luminescence (OSL) dating of quartz to constrain the age of colluvial wedges preserved in a major branch of the AFS at the Mejillones Peninsula (Mejillones Fault) providing a recurrence interval of 3.5 + 3.5 Ka[7]. However, quartz in the Atacama Desert has poor luminescence dating properties due to its low OSL sensitivity, consequently the obtained ages are unreliable[8] and the recurrence interval remains a matter of debate. In addition, the recurrence interval of great subduction earthquakes in northern Chile is poorly constrained; based on instrumental data, a 115-year-return period for M > 8.0 earthquakes has been proposed for this part of the Chilean subduction margin[9].

[1]National Research Center for Integrated Natural Disaster Management (CIGIDEN), Departamento de Ciencias Geológicas, Universidad Católica del Norte, Avenida Angamos 0610, Antofagasta, Chile. [2]Institute of Geosciences, University of São Paulo, Rua do Lago 562, São Paulo, SP 05508-080, Brazil. [3]Geology Department Middlebury College, Middlebury, Vermont 05753, USA. [4]Escuela de Ciencias del Mar, Pontificia Universidad Católica de Valparaiso, Avenida Universidad 330, 2340000 Valparaiso, Chile. ✉email: ggonzale@ucn.cl

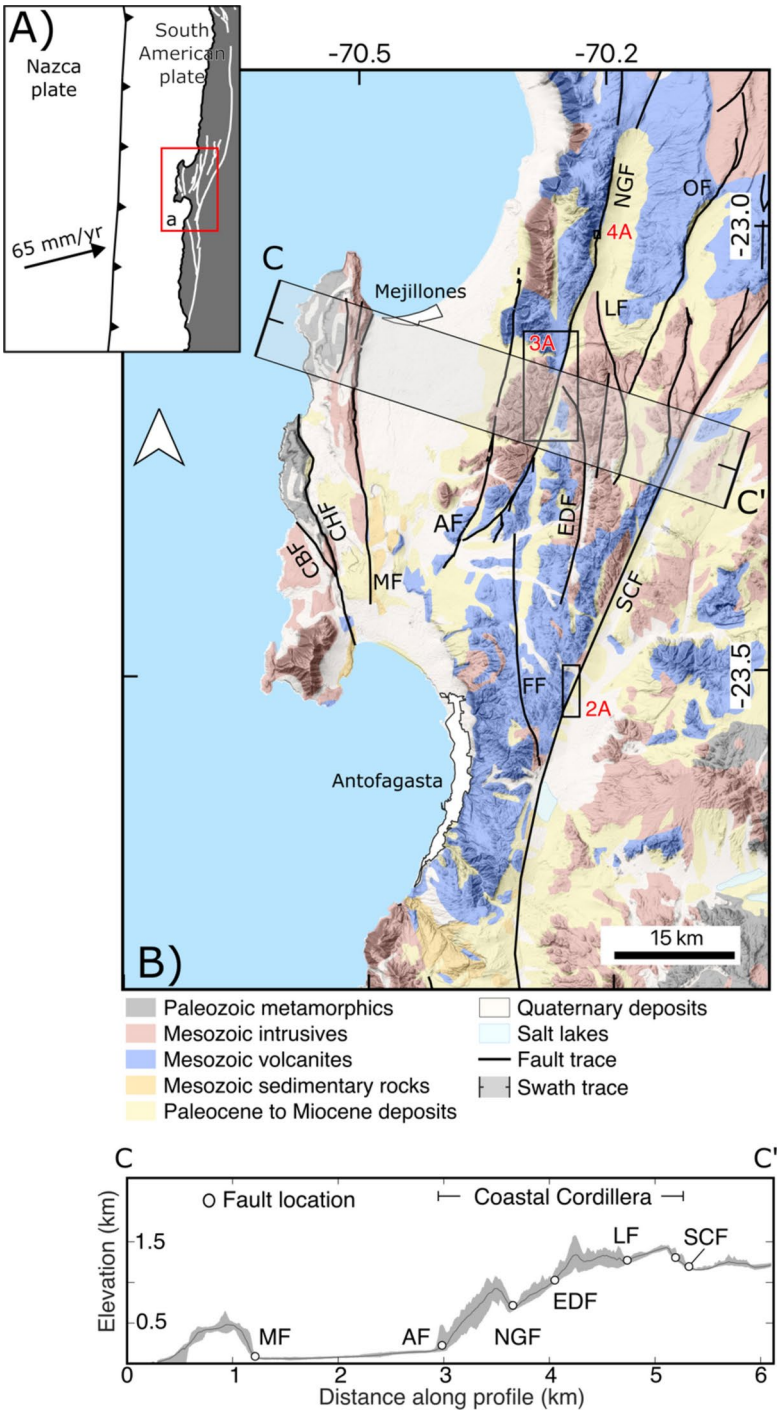

Based on palaeoseismological trenching we reconstruct the slip rate and the recurrence time of earthquakes in two branches of the AFS, the salar del carmen fault (SCF) and the Naguayán Fault (NGF). The surface ruptures were characterised by the inspection of the Google Earth platform and high-resolution digital elevation models (HR-DEMs) developed using unmanned aerial vehicles and structure from motion techniques[10]. Additionally, we levelled several topographic profiles using a dual GPS. To better constraint recurrence interval of surface rupture earthquakes, we use post-infrared infrared stimulated luminescence (pIR-IRSL) dating of potassium feldspar from colluvial wedges and Late Pleistocene sedimentary deposits following Del Rio et al.[8]

Long-term and quaternary deformation of the AFS

The AFS extends more than 1000 km in the northern Chile forearc (20 and 30°S)[8]. This fault system originated as a left-lateral trench-parallel fault system during the Early Cretaceous[11]. In the surroundings of Antofagasta, the major branches of the AFS strongly control the topography (Fig. 1). Generally, the faults show fault dip variations between 70° and 80° to the east. Since the Miocene, these structures have been dominated by vertical displacements defining up to 650 m in high mountain fronts in the Coastal Cordillera[5,12–15] (Fig. 1B). East-facing fault scarps and open fractures preserved in Pliocene–Pleistocene alluvial deposits are common in the piedmont

◀**Fig. 1**. Tectonic, geological and structural setting of the Atacama fault system. (**A**) Tectonic setting of the AFS, white lines show main branches of the AFS, black line with triangle represent the trench of northern Chile subduction zone. (**B**) Geological and structural setting placed on shaded relief derived from an ALOS Palsar 12.5 m DEM showing the distribution of major faults conforming the AFS in the surroundings of Antofagasta. Black lines represent fault-controlled mountain fronts formed by the AFS along which fault scarps are discontinuously developed in Quaternary alluvial deposits. Fault acronym: *CBF* caleta bandurrias fault, *CHF* caleta herradura fault, *MF* mejillones fault, *AF* aeropuerto fault, *NGF* naguayán fault, *FF* fortuna fault, *EDF* el desesperado fault, *LF* laguna fault, *OF* ordóñez fault, *SCF* salar del carmen fault. (**C**) Topographic swath profile CC'. Note that major topographic changes occur at the intersection with the major faults. Sites 1, 2 and 3 indicate the locations of the SCF-1, NGF-1 and NGF-2 palaeoseismological trenches, respectively. The swath trace of the profile presented in C shows the fault-controlled topography and was derived from an ALOS Palsar DEM. Maps were elaborated using QGIS-LTR 3.4 (www.qgis.org/). Plate boundaries presented in A where obtained at http://peterbird.name/oldFTP/PB2002/, emerged land data was downloaded from www.naturalearthdata.com. The geological units presented in B correspond to the Geological Map of Chile 1:1.000.000 (free available https://tiendadigital.sernageomin.cl/es/geologia-basica/864-2002mapa-geologico-de-chile-escala-1-1000000-n-mapa-m61.html). The ALOS Palsar DEM was downloaded from https://www.geoportal.cl/geoportal/catalog/download/f77f1be6-3dfc-37ce-a689-3f72022d301f. The Swath profile presented in C was calculated in MATLAB R2023b with an educational license. Final edition of the figure was made using Inkscape 1.4 (www.inkscape.org/).

of these mountain fronts (Fig. 2), attesting to the most recent reactivation. The kinematics of the youngest displacements of the AFS are controversial, it has been interpreted as either the result of left-lateral motion[16] or normal faulting[14,15,17]. We observed by using digital elevation models and field inspection that normal faulting dominates in fault segments striking N–S, whereas faults striking NE–SW exhibit a sinistral strike-slip lateral component and normal faulting.

Results

The main scarp of the SCF

At the scale of the Coastal Cordillera this fault is expressed by a mountain front exceeding 100 km of length and up 560 m in high. The scarp marking the youngest activity of the SCF is preserved in the Pliocene–Pleistocene alluvial deposits and extends for 40 km at the piedmont junction with the mountain front. The scarp represents a multi-segmented fault rupture (Fig. 2A y2B), composed of three major fault segments, although subsegments are involved in each fault segment. The subsegments are joined by relay ramp structures and display mainly east-facing scarps (Fig. 2B). The northernmost segment strikes N20E, the central segment strikes N18E and the southern segment N08E. The northernmost segment is covered by the paleoseismological analysis of this contribution. This segment crosscuts an older west-facing fold scarp formed by reverse faulting (Figs. 2B–D). In fact, we observed in several localities the occurrence of reverse faults and folds cut by the youngest reactivation of the SCF that led to the formation of the east-facing scarp (Fig. 2D).

An abandoned alluvial surface is exposed to the west of the main fault scarp of the SCF. It forms a faulted continuous piedmont inclined ~ 3 to 5° to the east along the eastern border of the Coastal Cordillera (Fig. 2B). This surface has accumulated an average offset of 5.4 ± 1.5 m across the entire rupture[14]. Because this piedmont does not show large topographic undulations, the average of surface offset is representative of the accumulated fault-slip. High-resolution profiles crossing the scarp show slope breaks, suggesting that the scarps grow through multiple events (Figure S1). At the trench site of the SCF (Fig. 1), we distinguished at least two bevels between the scarp head and the scarp crest, identifying at least two degradation stages of the scarp profile. The scarp profile is dominated mainly by debris slopes (20–30°); however, the local occurrence of slopes > 50° indicates the preservation of the free face, which is highly favoured by the presence of a gypsic soil (Fig. 6A). The lower portion of the scarp exhibits slopes between 3–5°. The fault plane of the SCF dips 70 ± 5° to the east, and the scarp face is also directed to the east; thus, the recorded east-side-down surface offset is consistent with normal faulting. In the segment where we excavated the trench, Armijo and Thiele[16] interpreted 60 to 100 m of sinistral displacement of the alluvial surface. The few pieces of evidence suggesting sinistral lateral offset are fractures stepping to the left with respect to the fault scarp trend and northwards channel migration in the upthrown block. In this case, the lateral component is not larger than 2.0 m from the channel incision (Figure S2).

The main scarp of NGF

The NGF is expressed by an up to 650-m high mountain front, west of the fault, delineating the local morphology for more than 55 km (Fig. 3A). The youngest displacements of the NGF are expressed by discontinuous fault scarps offsetting Pliocene–Pleistocene alluvial deposits (Fig. 3B,C,D y E). In its northern section, the NGF exhibits a 22 km-long single mountain front with an 8-km long older reverse fault scarp facing mainly to the west in its central part (Fig. 4A). The central section of the NGF is characterized by an east-facing fault scarp, which trends N25°E continuously expressed for 19 km trending; in the northern most section, the NFG shows a local inflection to the N–S direction (Fig. 3A). The southern extension of the NGF is formed by discontinuous fault scarps aligned along the fault trace of this structure.

In the central section of the NGF we carried out the palaeoseismological study. In this section, the fault plane dips 67 to 80° to the east. Where the scarp retains a N–S direction, the local morphology shows east-side down normal displacement given by a piedmont surface preserved at the top of the fault scarp. The average surface offset of this surface is 2.7 ± 0.8 m. It was obtained from high-resolution profiles extracted from HR-DEMs

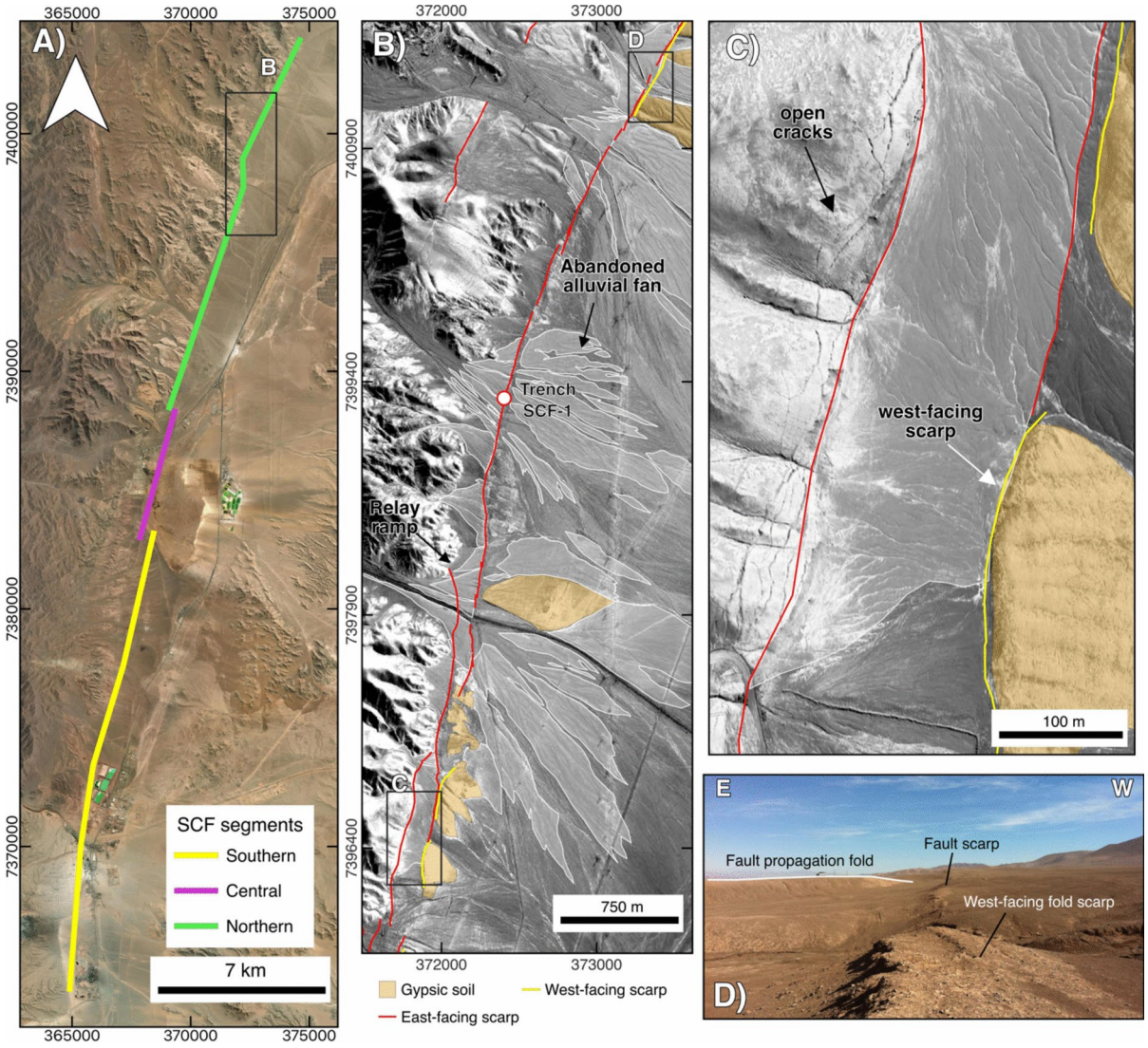

Fig. 2. Details of the SCF trace. (**A**) Three main fault segments configuring the east facing fault scarp of the SCF. Note the alluvial fans forming the piedmont affected by the fault segments. (**B**) Main trace of the SCF showing three fault scarps overlapping along strike and forming relay ramp structures. Note the abandoned alluvial fans (outlined by white lines) displaced by the east-facing scarps. Orange represents gypsic soil surfaces uplifted by west-facing fold-scarps. Black dot represents the location of the SCF-1 trench. (**C**) Detail of open cracks formed in gypsic soil developed in colluvial sediments of the Coastal Cordillera. Dark surfaces represent abandoned alluvial fans. (**D**) Southward view of the SCF scarp at its northern tip. At this place, the normal fault scarp crosscuts a west-facing fold scarp formed by older reverse faulting.

(Figure S1). In this place, we also observed a fault-propagation fold in the footwall of NGF (Fig. 4B). Because this fold is cut by the later normal faulting, the fold represents an older phase of reverse faulting.

In the same central section, where the NGF strikes N25E (Fig. 3C), there is a dislocated alluvial surface showing several fluvial channels sinistrally displaced (Fig. 5A,B). The lateral displacement varies between 4.3 and 5 m, with a mean value of 4.65 ± 0.46 m. This mean value was obtained from six laterally displaced channels along a 1 km long fault segment. The height of the scarp ranges between 0.10 and 2.3 m, this variation is given by the occurrence of a displaced palaeotopography. An interesting aspect of this paleotopography is the occurrence of an older fault scarp facing to the west, which is related to an older episode of reverse faulting along the NGF, which uplifts the eastern side of the fault (Fig. 5C).

Palaeoseismological evidence of near-surface rupture earthquakes

In the SCF, the trench site was excavated across the east facing fault scarp in the northernmost segment (Fig. 1). In the NGF, we selected two sites for trenching in the central section of this fault: a northernmost site (NGF-1, Fig. 3B) is dug in a N–S-striking fault segment where the fault forms an east-facing normal-fault scarp. The second trench site (NGF-2 in Fig. 3C) is in a N25E-trending fault segment, where the sinistral offset of

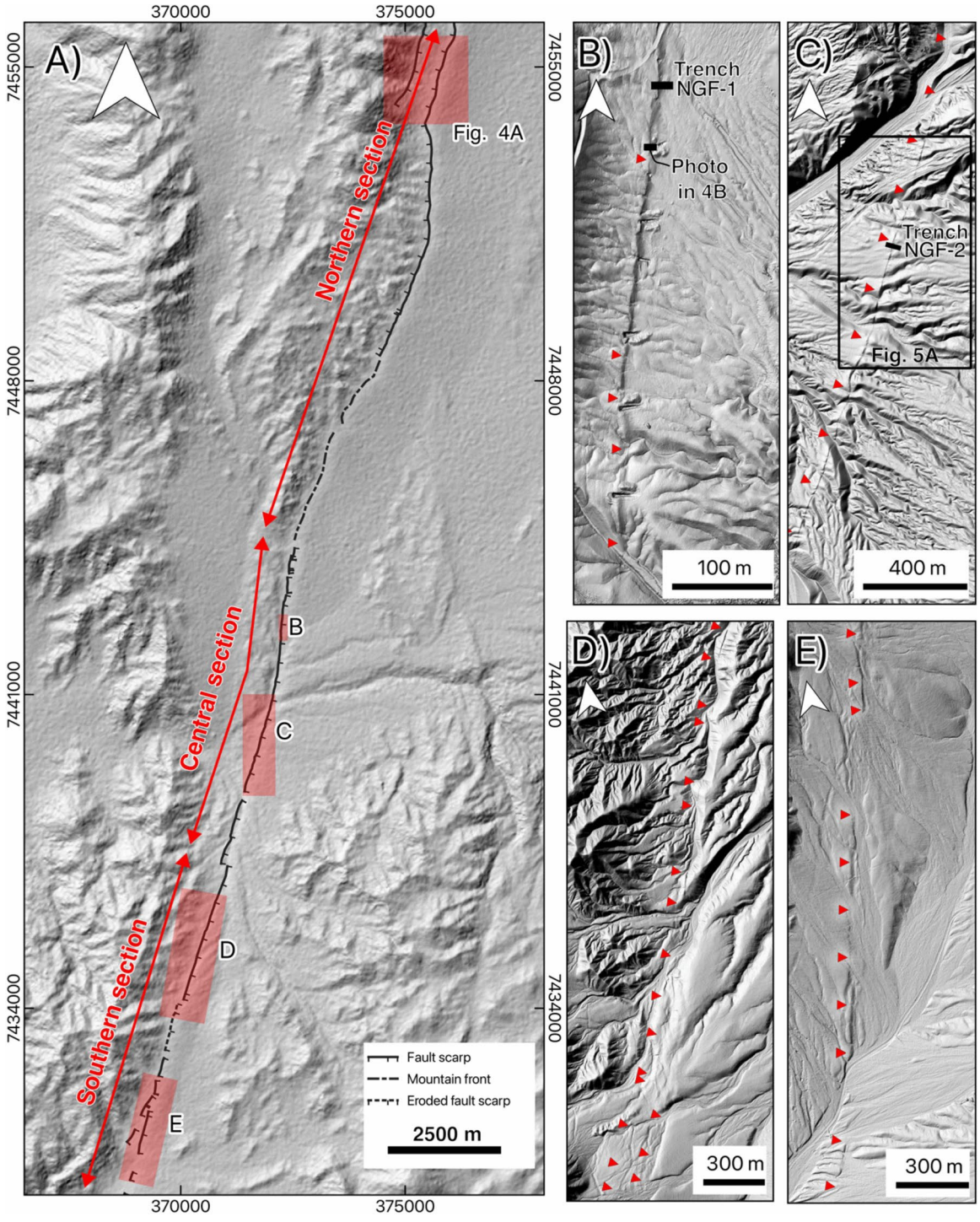

Fig. 3. (**A**) Hill Shade image based on ALOS Palsar 12.5 m DEM showing the three sections of the Naguayán fault trace. (**B**) Hill Shade Image based on HR-DEM showing normal fault scarp of the central section, (**C**) Hill Shade image based on HR-DEM depicting fault scarp formed on alluvial surface with lateral displaced fluvial channels. (**D**) Hill Shade image based on HR-DEM showing fault scarp in the southern section. (**E**) Hill Shade image based on HR-DEM illustrating west facing scarp in the southern section.

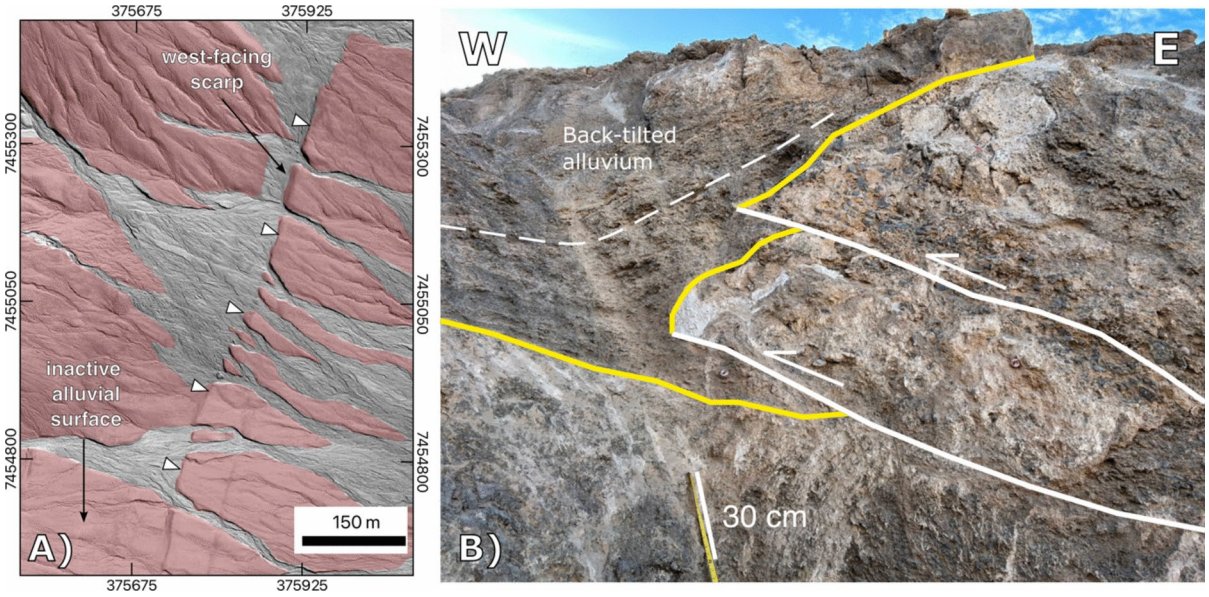

Fig. 4. Field evidence for reverse faulting at the NFG. (**A**) Satellite imagery of the northern extent of the NGF. At this site, reverse displacements have constructed a west-facing scarp that has promoted the preservation of the inactive alluvial surface at the hanging wall of the fault. (**B**) Northern wall of an exploratory trench near trench NGF-1. At the trench wall, two east-dipping reverse faults displace alluvial gravels with gypsic soil at the top, and progressive tilting of the surface is evidenced by the back-tilted alluvial layers covering the soil.

alluvial channels is well expressed. Trench stratigraphy, units, and sedimentological details are described in the supplementary material.

The SCF-1 trench

This trench was planned to expose the stratigraphy of the scarp-derived deposits, which conform to the debris slope and the wash slope section of the fault scarp. The logged wall dimensions are ca. 9 m long and 3.5 m deep at its deepest point, next to the fault plane (Fig. 6A). The surface offset in the trench site is 5.6 m that matches very well with the average 5.4 ± 1.5 m surface offset.

The stratigraphic expression of earthquakes in the trench wall is given by three colluvial wedge deposits termed CW1, CW2, and CW3 (Fig. 6B). These colluvial units form the talus of the fault scarp, taper to the east and stack vertically, indicating that they were generated by fault scarp degradation. Colluvial wedge thickness (Table 1) were measured by using a measuring tape directly in the trench-wall, above the main fault and parallel to the buried portion of the fault scarp. The bottom of the colluvial wedges is well expressed by soil development and/or angular unconformities. The main fault dips 68° to the east and displaces the four oldest stratigraphic units of the trench (GS, FS, CW1, and CW2 in Fig. 6B); CW3 seals the fault activity in the trench exposition. The SCF in the trench site has accumulated ca. 6.2 m along-dip displacement (Fig. 6A).

The CW1 and CW2 are displaced by secondary, synthetic, and antithetic faults. These faults define two graben structures (Figure S4). Deformation concentrates at the borders of the grabens, reaching vertical displacements of up to 0.3 m. The internal deformation of the grabens is characterised by deformation bands, which drag and rotate the laminated structure of CW2 (Figure S4D,E). The localised subsidence in the graben created a small depression filled with laminated sands accumulated on top of CW2 (Figure S4D,E). The secondary faults defining the boundaries of the grabens are restricted to GS, CW1, and CW2, and the overlaying CW3 unit is not affected by these structures. On both sides of the eastern graben, discontinuous fractures and deformation bands are well developed in the laminated sands of CW2.

Given the standard convention that the maximal colluvial wedge thickness approaches to the half of coseismic along-dip slip[18] we estimate 1.6 ± 0.06 m for CW1, 2.0 ± 0.05 m for CW2 and 2.4 ± 0.04 m for CW3. The error represents variation in the measurements of the colluvial wedge thickness done in the two trench walls. The 6.2 m of along-dip accumulated displacement matches very well with the 6.0 ± 0.15 m obtained by the summation of the coseismic slips. Considering the 6.2 m along-dip the fault and the lateral offset of 2 m we obtain a rake angle of 72° for the cumulative displacement. Using this rake, we obtained an accumulated net slip of 6.5 m, and coseismic net-slip of 1.7 ± 0.04, 2.1 ± 0.03, and 2.5 ± 0.02 m for the first, second, and third earthquakes, respectively. We considered that the coseismic net-slip represents an average surface displacement (AD) instead of maximum displacement (MD). It is because the surface offset in the trench site matches the average surface offset along the total surface rupture. According to empirical relations[19] between AD and moment magnitude (M_w), the estimation for the first earthquake is M_w 6.9 ± 0.1, for the second earthquake M_w 7.0 ± 0.1, and for the third earthquake M_w 7.0 ± 0.3 (Table 1). An independent estimation of M_w 7.0 is given by the preserved surface rupture length (SRL), which is ca. 42 km.

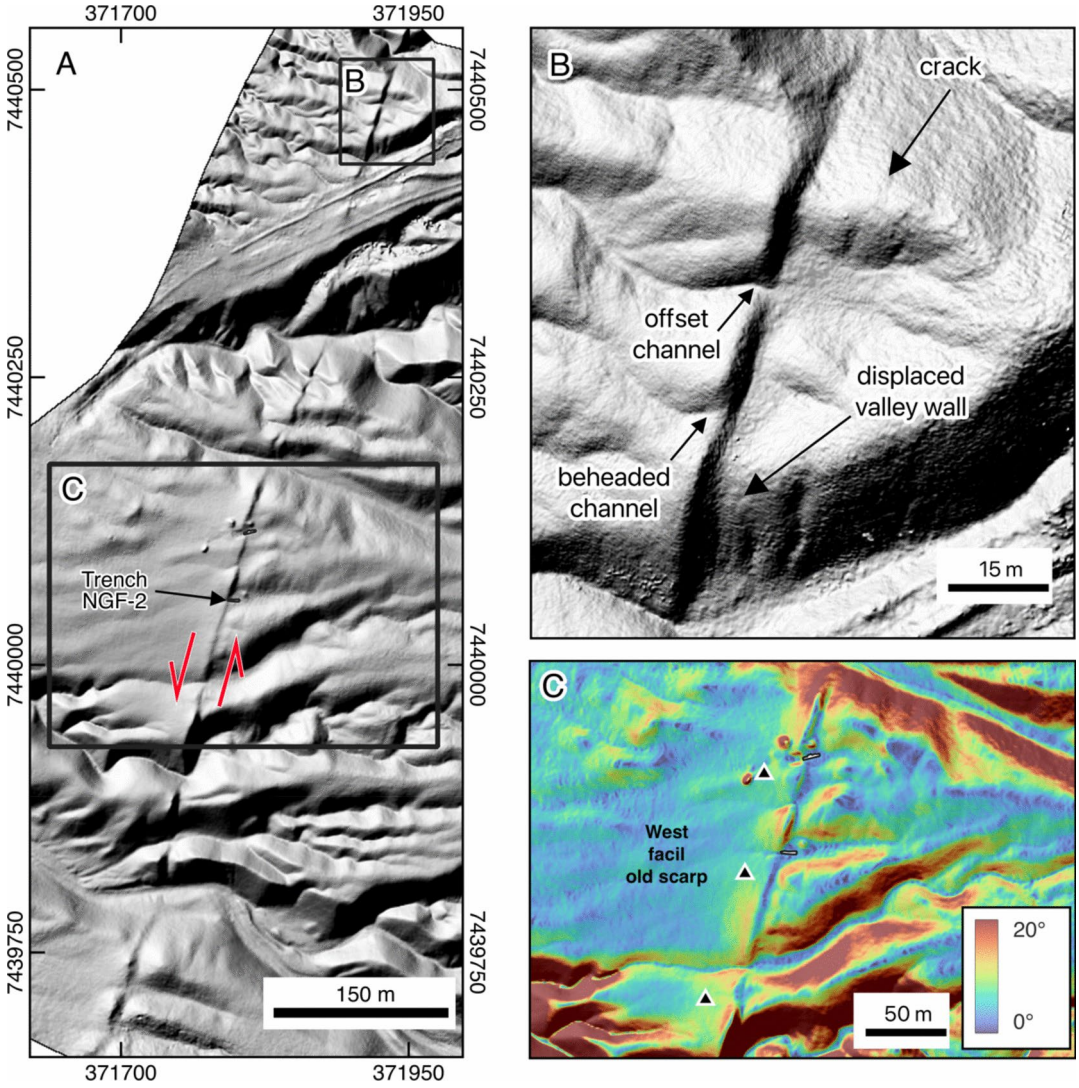

Fig. 5. Map views of the NGF-2 trench area. (**A**) Main trace of the NGF showing sinistral offset of morphological features, (**B**) details of beheaded and offset channels, and (**C**) slope map showing topographic bench along the fault trace of NGF. This bench has a slope facing to the west (black triangles) that is opposite to the east-facing scarp promoted by the youngest displacement events along the NGF in this trench site.

The NGF-1 trench

The trench is ca. 14 m long, ca. 6 m deep and crosses perpendicular to the fault scarp (Fig. 7A). The main fault dips 80° to the east at the trench site. The trench exposes three events: the first event is related to the aperture and infill of the older cracks (Crl in Fig. 7B), the second event is inferred by the occurrence of a partially eroded colluvial wedge (CW1d and CW1w in Fig. 6B), and the third event is expressed by the cutting relationship between the colluvial wedge and the main fault. In fact, CW1d is clearly displaced by the fault; a depositional contact is discarded due to the subvertical character of the contact angle between CW1d and alluvial gravels. Based on the position of a gypsic soil (GS in Fig. 7B) on both sides of the fault, we determined a net normal offset of 3.8 ± 0.1 m. Due to the occurrence of a colluvial wedge, we inferred that the second event was an earthquake, which ruptured the topographic surface. Using the thickness of the partially eroded colluvial wedge, we estimate a minimum coseismic displacement of 2.2 m corresponding to a minimum M_w of 7.1 earthquake (Table 1). The fact that the main fault cuts this colluvial wedge as second event. The total displacement of the tip point through the colluvial wedge was 1.1 m. The net offset measured in the trench was 3.8 m, so the total slip accumulated by these two events was 3.3 m, and the remaining 0.5 m of offset is the result of the underestimation of the coseismic displacements using a partially eroded colluvial wedge.

The NGF-2 trench

Trench NGF-2 is 8 m long and 1.65 m deep (Fig. 8), and it is excavated in the fault-downgoing block along a laterally displaced channel filled with aeolian and alluvial sandy deposits (AD1, AD2 and AD3 in Fig. 8A). The channel is incised in the Plio-Pleistocene gravels (AGs in Fig. 8A). Near the fault, the sedimentary infill

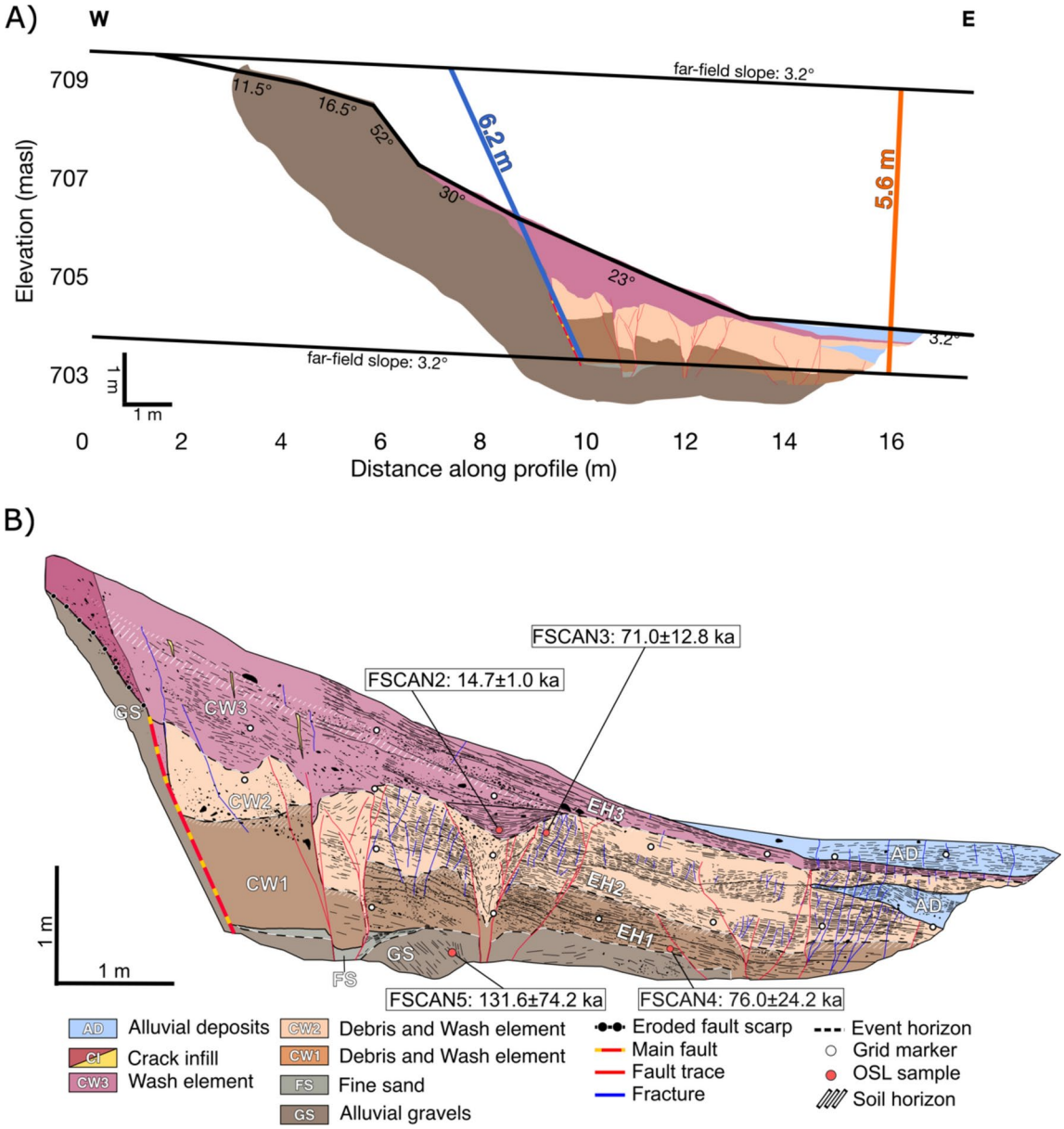

Fig. 6. Exposition of the SCF and deformed sediments in SCF-1 trench. (**A**) Geometry of the scarp at the northern wall of the trench. The slope angles of the scarp profile are given in degrees. Angles were obtained from 1–2 cm high resolution topographic profiles using dual GPS. Far field slope angles were extracted from a longer high-resolution topographic profile, which is not presented in the figure. The yellow line corresponds to the surface offset (5.6 m), which implies a 6.2 m along-dip displacement. (**B**) Logging of the northern wall of trench SCF-1. OSL ages are presented in black.

of the channel is accommodated in a graben structure limited to the west by the main fault and to the east by a subvertical fault (Fig. 8A). The main fault dips 70° to the east; it puts in contact the sedimentary infill of the channel (AD1 and AD2 in Fig. 7A) with the strongly cemented displaced alluvial gravels (AGs) located to the west of the fault. Fault activity has conducted ca. 1.75 m of along-dip displacement of the AGs unit (Fig. 8B). In the graben structure, there are several east-dipping deformation bands that displace AD1 and AD2. The deformation bands produce along dip separations of 10 to 2 cm in the layers of AD1 and 5 to 1 cm in the layers of AD2. AD1 is 23 cm thicker in the graben than outside the graben, and AD2 is 32 cm thicker in the graben (Fig. 7B). Both thickness differences indicate that the accumulation space was created by a narrow deformation in the graben.

In the NGF-2 trench, we interpret two earthquake events: the first earthquake blocked sediment transport along the channel, enabling the accumulation of the AD1 unit. Subsequent syndepositional subsidence at the graben and/or the lateral offsets produced the thickness difference between the AD1 unit in the graben and outside the graben. A second earthquake increased the scarp height and tilted the AD1 layers. The vertical offset produced by this earthquake enabled the accumulation of unit AD2 in the channel. Later, the graben located east

Fault	Trench	Slip sense	Unit	Thickness [m]	Dip slip [m]	Net slip [m]	Mw (AD) *Mw(Av)
SCF	SCF-1	Normal	CW1	0.8 ± 0.05	1.6 ± 0.06	1.7 ± 0.04	6.9
		Normal	CW2	1.0 ± 0.05	2.0 ± 0.05	2.1 ± 0.03	7.0
		Normal	CW3	1.2 ± 0.05	2.4 ± 0.04	2.5 ± 0.02	7,0
NGF	NGF-1	Normal	CW1g	1.0 ± 0.05	2.0 ± 0.05	2.2 ± 0.05	7.0
	NGF-2	Strike-slip	AD1	0.5 ± 0.05	0.5 ± 0.05	2.2 ± 0.5	7.2 ± 0.1*
	NGF-2	Strike-slip	AD2	0.6 ± 0.05	0.6 ± 0.05	2.6 ± 0.5	7.3 ± 0.1*

Table 1. Summary of geometrical measurements used for estimation of paleomagnitudes. M_w(AD) magnitude estimated using net slip as average displacement and *M_w (Av) magnitude estimated as an average between the M_w(AD) and M_w(MD).

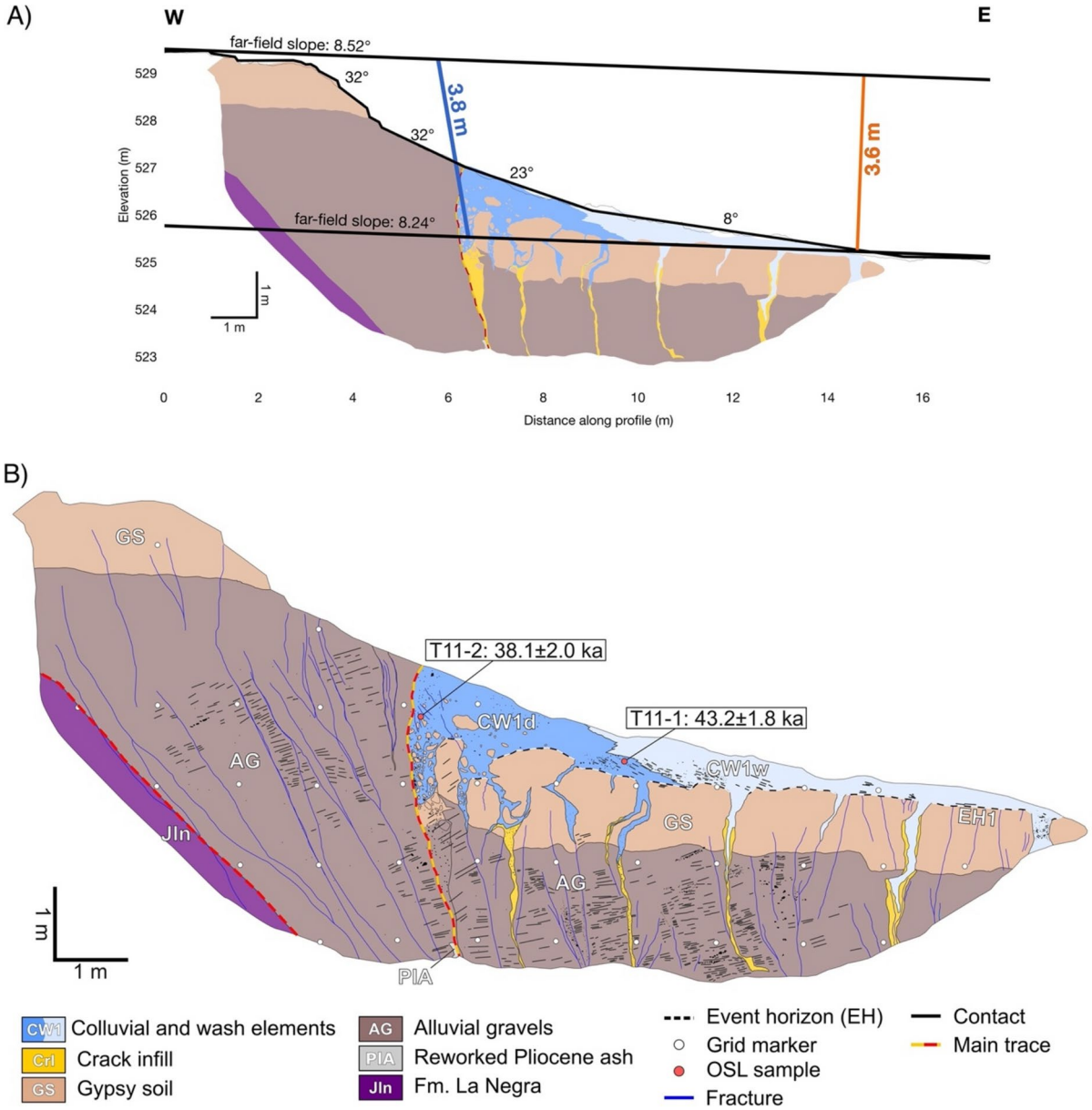

Fig. 7. Exposition of the NGF and deformed sediments in NGF-1 Trench. (**A**) Geometry of the scarp; the slope angles of the scarp profile are given in degrees, black lines represent the surface offset of the topography, and blue lines represent the offset of the gypsic soil. Far field slope angles were extracted from a longer high-resolution topographic profile, which is not presented in the figure. (**B**) Logging of the southern wall of trench NGF-1.

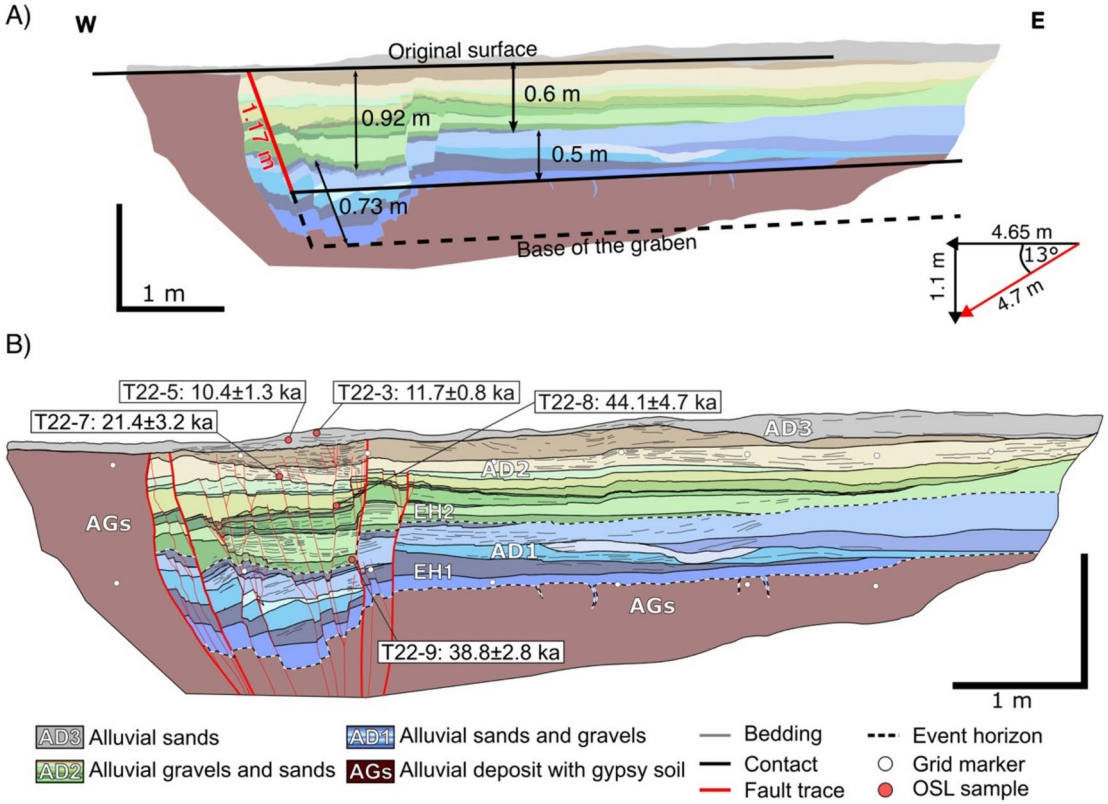

Fig. 8. Exposition of the NGF and deformed sediments in NGF-2 Trench. (**A**) Logging of the northern wall of trench NGF-2 at the Naguayán Fault. The obtained OSL ages are presented in black. (**B**) Measurements of unit thickness and displacements at the trench. Unit thickness is depicted with black lines. The red solid line depicts the along-dip separation of the AGs unit. The red dashed line depicts the along-dip separation conducted by the fault considering the creeping-like displacements. The inset depicts the accumulated net offset of the NGF estimated considering the dip- and strike-slip components estimated from stratigraphic and geomorphic markers, respectively. The acute angle corresponds to the rake of the slickenside.

of the main fault experienced subsidence generating the thicker accumulation of AD2 within the graben. The sedimentation of AD1 and AD2 was contemporaneous with the activity of the deformation bands (Figure S4D). The top of AD2 is cut by at least three deformation bands and the boundary between AD2/AD3 does not exhibit an offset, therefore sealing the deformation.

Using the accumulated lateral displacement and the accumulated vertical displacement from the stratigraphic infill outside the graben (Fig. 8A) we determined 4.7 ± 0.03 m of cumulative net displacement and estimate a rake angle of 13 ± 5° N. This cumulative net displacement represents the combination of two earthquakes. In this calculation, we discard the thickness difference between AD1 and AD2 inside and outside the graben, because it represents a narrow deformation controlling graben subsidence not connected with seismic processes. We estimated the along-dip slip of each earthquake using the thickness of units AD1 (0.5 ± 0.05 m) and AD2 (0.6 ± 0.05 m) outside the graben. We assumed in this estimation that the scarp acted as a trap for AD1 and AD2 accumulation. Using the rake as the slip vector and the vertical offset of each earthquake, we estimated a coseismic slip of 2.2 ± 0.5 m and 2.6 ± 0.5 m for the first and second earthquakes, respectively. Using the coseismic slip as average displacement (AD) and the empirical relationship between AD and M_w[19] the surface rupturing earthquakes reached M_w(AD) of 7.3 ± 0.1 and 7.4 ± 0.1 respectively. If the coseismic slips are considered as maximal displacement (MD), the estimated M_w(MD) is 7.05 ± 0.05 and 7.15 ± 0.05 for both earthquakes respectively. We are not able to discriminate between these two options; thus, we express the estimation of M_w as the average of AD and MD resulting 7.2 ± 0.1 for the first event and 7.3 ± 0.1 for the second event (Table 1).

Luminescence dating, age model and earthquake recurrence

We constructed age models for the stratigraphic record of each trench based on the post-infrared infrared stimulated luminescence at 225 °C ($pIRIR_{225}$) ages of potassium feldspar from Del Río et al.[8] (Table S1) and ages obtained in this work (Table S2) and a 351 ± 181 ka ^{21}Ne exposure age for the alluvial surface of the SCF-1 site[17]. Details of sample collection, preparation and laboratory procedures are found in the supplementary material. The models were constructed using OxCal[20], a tool developed to perform analysis of chronological data considering stratigraphic constraints by means of Bayesian statistics. The OxCal age model uses numerical ages and a conceptual geological model for defining the stratigraphic evolution. In all the trenches, we could draw a

palaeoseismological evolution in which we distinguished discrete-sudden slip events interpreted as earthquakes as the main control of sedimentation.

In the SCF, we identified three ~ M_w 7.0 earthquakes. The first earthquake marked the beginning of scarp formation and was related to the event horizon EH1 in (Fig. 6B). The ^{21}Ne age and the $pIRIR_{225}$ age of FSCAN5 are the maximal ages for this event horizon. The minimal age of EH1 was defined by the age of FSCAN4 obtained in CW1. The modelled age of EH1 was 100 ± 28 ka (Table S3) and represented a temporal constraint for the beginning of the CW1 accumulation and the age of the first earthquake. A second earthquake was expressed by the event horizon EH2 between CW1 and CW2. According to the age model, EH2 has an age of 78 ± 14 ka (Table S3). The third earthquake was interpreted from the contact between CW2 and CW3 (EH3) with a modelled age of 59 ± 17 ka (Table S3). This event was sealed with the deposition of CW3. The later accumulation of CW3 was given by the graben infill above the hourglass structure, which according to the age model was deposited at 16.7 ± 1 ka (FSCAN2 in Table S3). Considering the 6.3 ± 0.05 m cumulative net displacement estimated for the SCF, we estimated a long-term slip rate of 0.06 ± 0.02 m/ky.

Because of the low number of ages, in the NGF-1 trench, we developed an age model for only trench NGF-2. In NGF-1, we could constrain the age of the three events relatives to the two available $pIRIR_{225}$ ages (T11-1 AND T11-2 in Table S2); the first event expressed by the deepest crack infill is older than 43 ± 2 ka. The ages in CW1 are likely near the age of the second earthquake, and the third event, expressed by the cutting relationship between the main fault and CW1, is younger than 43.2 ka.

In trench NGF-2, we identified two event horizons: EH1 is inferred by the unconformity separating AGs from AD1, and EH2 by the unconformity between AD1 and AD2. EH1 represents the ground surface over which AD1 was deposited due to the presence of the fault scarp. Although we did not have any numerical age near the base of AD1, we could estimate this age by considering the sedimentation rate of 0.039 m/ky of AD2 (Figure S12). This rate was estimated considering the time (Table S4 and Figure S11) and vertical distance between samples T22-7 and T22-9 (Fig. 7A). Using this sedimentation rate and the modelled age of EH2, the base of AD1 has an age of 66 ± 5.5 ka, which is the age of the first palaeoearthquake (M_w 7.1) in the trench record. The second palaeoearthquake (M_w 7.2) rotated the AD1 layers and produced the normal separation of the same layers. According to the age model, this event has a modelled age of 42 ± 2.9 ka (EH2 in Table S4). Following EH2, AD2 was deposited sintectonically inside the graben. The deformation of AD2 is sealed by the deposition of AD3 at 14.6 ± 1.1 ka (AD3 in Table S4). We interpreted that the palaeoearthquake recognised in the NGF-1 trench was the same earthquake that tilted the AD1 layers in the NGF-2 trench. By estimating the overlap between the probability density functions for both events, we obtained a better constrained age for this event of 42 ± 2 ka (Figure S11). Using the net offset of 4.7 ± 0.03 m and the age of this first earthquake of 66 ± 5.5 ka, we calculated a slip rate of 0.07 ± 0.006 m/ky.

Because of the large uncertainty of the ages, we could not use the simple difference between the earthquake ages for the recurrence interval estimation. In its replacement, we used the following relation[18].

$$RI = D/S.$$

where RI is the recurrence interval, D is the mean coseismic slip, and S is the slip rate. The 0.06 ± 0.02 m/ky slip rate of the SCF and the mean vertical component of the coseismic slip of 2.1 ± 0.03 m enabled us to calculate a recurrence time of 35 ± 12 ky for M_w 7.0 ± 0.1 earthquakes. Using the slip rate of 0.07 ± 0.006 mm/yr of the NGF and the average coseismic slip of 2.4 ± 0.3 m obtained in the trench site NFG2, we calculated a recurrence time of 34 ± 5 ky for Mw 7.1 ± 0.1 earthquakes.

Discussion

In this work we have demonstrated that the later activity of the AFS is related to upper plate extension, which caused surface rupture earthquakes, forming fault scarps in Quaternary alluvial deposits. Upper plate normal fault reactivation in Chile and Japan has been clearly demonstrated as transitory stress relaxation of the overriding plate imposed by complete decoupling of the megathrust[1,2]. As we noted in the fault scarp description of the SCF and NGF, reverse faulting was active before normal faulting implying that these faults have reversed their kinematics from reverse faulting to normal faulting during the most recent time. Previous works have described similar findings in other branches of the AFS and interpreted this reverse faulting is related to the compressive deformation induced in the upper plate during the interseismic stage of subduction earthquake cycle[5]. Our detailed structural observations are not conclusive about this idea. Nevertheless, we observe that extensional deformation is the driving factor controlling the morphology of the Coastal Cordillera. This reflects that, in the long-term record, since the Miocene[5,12], the landscape configuration has been dominated by normal faulting, showing that the geomorphological imprint of the coseimic and postseismic stages of subduction earthquakes is more efficient than the interseismic stage.

The later activity of the AFS, creating east facing fault scarps, reflects the occurrence of 7.0–7.4 M_w palaeoearthquakes, implying coseismic ruptures of approximately 40 km in length. Using the relation between magnitude and area, we conclude that the entire brittle domain was seismically active during these events. Previous studies[7] in the Mejillones Fault arrive at a similar conclusion. However, a contrasting point is the age of the individual events. As we noted, age constraint of the later activity of the AFS is limited to the use of OSL in quartz, which provide unreliable ages due to the poor luminescence properties of quartz[8]. Our age constrains indicate that the later displacements in the AFS are older than previous estimates, having lower slip rates and longer recurrence intervals. In particular our slip rates and recurrence interval estimations are one magnitude order higher and longer respectively than the previous estimation allowing to characterize these faults as slow faults. In the study area, there are ten upper plate faults forming fault scarps like the SCF and NGF. We determined the recurrence of the whole fault system by assuming that each individual fault has a recurrence of

35 ± 9 ky. This calculation bases on the probability that one of these ten faults reactivates in a specific year; then, we calculated the inverse of this probability. It provided a recurrence of 3.5 ± 2.8 ky for the system.

Upper plate normal fault reactivation after large subduction earthquakes in Chile and Japan has been clearly demonstrated as response of stress relaxation of the overriding plate[1,2] introducing the idea that this normal faulting is a direct result of large-to giant- subduction earthquakes. However, the NFG and SCF faults have an extremely long recurrence interval that exceeds approximately three hundred times the 115 years of recurrence for M > 8.0 subduction earthquakes in northern Chile[9] showing that recurrence times of large to giant subduction earthquakes and the studied faults are not synchronized. However, it must be considered that the previous given recurrence was estimated based on a poor instrumental record of subduction earthquakes. In the Itozawa Fault, Japan, the recurrence intervals of surface rupturing earthquakes are three to seven times longer than the interval of M > 9.0 subduction earthquakes[3] and in the Pichilemu Fault in central Chile, is ten to twenty times larger than M > 8.5 subduction earthquakes[4]. The observed asynchrony suggests that upper plate normal fault reactivation is a complex process in which several driving factors interplay. Previous studies have demonstrated that the reactivation depends on the position of the upper plate faults with respect to the magnitude and slip distribution of the earthquake on the megathrust[21]. These studies consider that there are few optimally orientated upper plate faults able to be reactivated as result of large and giant subduction earthquake. In this regard, the unclamping of optimally orientated faults depends on the coulomb stress change (CSC) imparted by subduction earthquakes[4,21]. In the Iwaki Fault, the CSC caused by the M9 earthquake was approximately three percent of the CSC needed for failure[22], revealing that the stress change on a given upper plate fault imparted by a single M > 9.0 subduction earthquake is not enough to reactivate it. Additionally, CSC analysis considering the interseismic and coseismic stages of the subduction earthquake cycle[23] has shown that the increase in coseismic CSC is counterbalanced by the interseismic stage suggesting that the complete unloading of a particular upper plate fault is sustained by the interplate contact during several subduction earthquake cycles.

Based on our estimation of the recurrence interval of M_w 7.0 earthquakes in the AFS, we suggest that the reactivation of upper plate faults occurs quasi-randomly after several cycles of great subduction earthquakes in a period of 3.5 ± 2.8 ky. The observed discrepancy between the recurrence time of subduction earthquakes and upper plate fault earthquakes could be due to the analysis focusing on individual faults rather than the entire fault system. Since in the estimation of the recurrence time of Mw 7.0 in the AFS as system we assume the recurrence time for individual faults is the same, which is not necessarily correct, we emphasize the importance of creating a more complete inventory of palaeoseismological data. This should include the recurrence intervals of large earthquakes in upper plate faults as well as those large to giant subduction earthquakes.

Concluding remarks

A relevant aspect for future analysis is to unravel whether subduction earthquake supercycles play a determining role in the reactivation of dormant upper plate faults. Subduction earthquake supercycles are long-term paroxysms between two minima of interseismic strains[24]. A limiting factor in defining earthquake supercycles is the lack of a long-term record of strain accumulation. We propose that the upper plate fault reactivation could represent a long-term strain indicator of the complete discharge of the elastic strain in the subduction megathrust. Therefore, addressing details of the long-term activity of upper plate fault could shed light on the duration of earthquake supercycles at subduction margins.

Methods

Preparation and mapping paleoseismological trench walls

Three trenches excavated with a rental tracked hydraulic excavator are the basis of our paleoseismological interpretation. The trench walls were cleaned and scraped off to remove major undulations. Then a 1 m × 1 m reference grid was marked in each trench wall. The grid defines vertical and horizontal reference lines, measured with a tape measure and a horizontal level. Grid nodes were marked by hammering nails in plastic bottle caps and then nailed in the trench wall. In order to have a georeferenced datum the position of each node was measured with a dual frequency GPS. Finally, we captured high resolution photographs of the trench wall. A georeferenced photomosaic of each trench wall was generated using structure from motion techniques[10]. The trench walls were described based on sedimentological and stratigraphic characteristics. To identify paleoearthquakes we use three combined criteria: i) identification of event horizons, ii) occurrence of colluvial wedges and iii) presence of stratigraphic unconformities. A key element in paleoearthquake identification was the observations of faults and fractures sealed by younger sediments. A complete description of trench wall stratigraphy is provided in the supplementary material.

Luminescence dating and age models

To constrain the timing of events and processes at the fault scarps, we date sediments extracted from the trenches following the post-infrared infrared stimulated luminescence at 225 °C ($pIRIR_{225}$) dating of potassium feldspar following procedures presented in Del Río et al.[8]. Samples were collected in two different sedimentary environments: the SCF-1 and NGF-1 trenches correspond to a classic normal fault scarp configuration with colluvial deposits at the base of the scarp related to its degradation. In contrast, the NGF-2 site corresponds to an outcrop-scale pull-apart basin filled with alluvial and eolian sediments. For the age models, we consider our samples and the ages presented in Del Río et al.[8] for the SCF-1 and NGF-2 trenches, and a ^{21}Ne age from González et al.[17] (Table S1).

Sediment samples were collected using steel tubes and were prepared following the protocol of Del Río et al.[8]. Samples T22-5, T22-8, and FSCAN-4 were analyzed in the Gamma Spectrometry and Luminescence Laboratory in the Instituto de Geociências at the Universidade de São Paulo (Brazil), using a Risø TL/OSL DA-20 reader system equipped with a ^{90}Sr/^{90}Y beta source, infrared and blue LEDs and filters for light detection in the blue

band using a photomultiplier. The samples (T11-1, T11-2, and T22-3) were analyzed in the Luminescence Laboratory of the Geology Department in Middlebury College (USA) using a Daybreak 2200 also with a $^{90}Sr/^{90}Y$ beta source. In Brazil, the samples were prepared in a room illuminated with subdued amber light. They were wet-sieved to acquire the 180–250 µm and treated with H_2O_2 and HCl (30%) to eliminate organic components and carbonates, respectively. Grains of potassium feldspar (K-feldspar, < 2.58 g/cm^3) were separated using a lithium metatungstate solution. After that, K-feldspar grains were treated with HF (10% for 40 min) to etch the alpha-irradiated outer layer, and a last treatment of HCl (30%) was applied to dissolve any possible fluoride precipitation. Washing and sieving was performed again to acquire K-feldspar concentrates target grain size (180–250 µm) for luminescence measurements (Details of luminescence dating in supplementary materials).

Data availability

Data is provided within manuscript of supplementary information. Additionally other data (digital elevation models and individual photos of the trench walls) can be requested to the corresponding author.

Received: 2 October 2024; Accepted: 14 January 2025
Published online: 23 January 2025

References

1. Toda, S. & Tsutsumi, H. Simultaneous reactivation of two, subparallel, inland normal faults during the Mw 6.6 11 April 2011 iwaki earthquake triggered by the Mw 9.0 Tohoku-oki, Japan, Earthquake. *Bull. Seismol. Soc. Am.* **103**, 1584–1602 (2013).
2. Farías, M., Comte, D., Roecker, S., Carrizo, D. & Pardo, M. Crustal extensional faulting triggered by the 2010 Chilean earthquake: The pichilemu seismic sequence. *Tectonics* https://doi.org/10.1029/2011TC002888 (2011).
3. Kimura, H. & Tsutsumi, H. Geologic and geophysical evidence of repeated normal faulting on the itozawa fault—The source of the Mw 6.6 iwaki earthquake triggered by the Mw 9.0 tohoku-oki megathrust earthquake, Northeast Japan. *Bull. Seismol. Soc. Am.* https://doi.org/10.1785/0120230030 (2023).
4. Jara-Muñoz, J. et al. The cryptic seismic potential of the pichilemu blind fault in Chile revealed by off-fault geomorphology. *Nat. Commun.* **13**, 3371 (2022).
5. Allmendinger, R. W. & González, G. Invited review paper: Neogene to quaternary tectonics of the coastal Cordillera, Northern Chile. *Tectonophysics* **495**, 93–110 (2010).
6. Arabasz, W. J. Geological and geophysical studies of the Atacama Fault System in northern Chile, Ph. D. thesis, 264 pp., Calif. Inst. of Technol., Pasadena. (1971).
7. Cortés, A. J. et al. Paleoseismology of the mejillones fault, Northern Chile: Insights from cosmogenic 10Be and optically stimulated luminescence determinations. *Tectonics* **31**, 1–21 (2012).
8. Del Río, I., Sawakuchi, A. O. & González, G. Luminescence dating of sediments from central Atacama desert, Northern Chile. *Quat. Geochronol.* **53**, 101002 (2019).
9. Comte, D. & Pardo, M. Reappraisal of great historical earthquakes in the Northern Chile and Southern Peru seismic gaps. *Nat. Hazards* **4**, 23–44 (1991).
10. Bemis, S. P. et al. Ground-based and UAV-based photogrammetry: A multi-scale, high-resolution mapping tool for structural geology and paleoseismology. *J. Struct. Geol.* **69**, 163–178. https://doi.org/10.1016/j.jsg.2014.10.007 (2014).
11. Scheuber, E. & Andriessen, P. A. M. The kinematic and geodynamic significance of the Atacama fault zone, Northern Chile. *J. Struct. Geol.* **12**, 243–257 (1990).
12. Naranjo, J. Interpretación de la actividad Cenozoica superior a lo largo de la zona de falla Atacama, Norte de Chile. Revista geológica de Chile. *Int. J. Andean Geol.* **31**, 43–55 (1987).
13. Niemeyer, H., González, G., Martínez-De, L. R. E., Martínez-Oe, E. & Ríos, L. Evolución tectónica cenozoica del margen continental activo de Antofagasta, Norte de Chile. *Andean Geol.* **23**, 165–186 (1996).
14. González, G. & Carrizo, D. Segmentación, cinemática y cronología relativa de la deformación tardía de la falla salar del Carmen, Sistema de Fallas de Atacama, (23° 40'S), Norte de Chile. *Revista geológica Chile* **30**, 223–244 (2003).
15. Delouis, B., Cisternas, A., Dorbath, L., Rivera, L. & Kausel, E. The Andean subduction zone between 22 and 25 S (Northern Chile): Precise geometry and state of stress. *Tectonophysics* **259**, 81–100 (1996).
16. Armijo, R. & Thiele, R. Active faulting in Northern Chile: ramp stacking and lateral decoupling along a subduction plate boundary?. *Earth Planet. Sci. Lett.* **98**, 40–61 (1990).
17. González, G., Dunai, T., Carrizo, D. & Allmendinger, R. Young displacements on the Atacama fault system, Northern Chile from field observations and cosmogenic 21Ne concentrations. *Tectonics* https://doi.org/10.1029/2005TC001846 (2006).
18. McCalpin, J. P. *Paleoseismology* (Academic press, 2009).
19. Wells, D. L. & Coppersmith, K. J. New empirical relationships among magnitude, rupture length, rupture width, rupture area, and surface displacement. *Bull. Seismol. Soc. Am.* **84**, 974–1002 (1994).
20. Bronk Ramsey, C. New approaches to constructing age models: OxCal4. vol. 14 http://c14.arch.ox.ac.uk/oxcal (2006).
21. Aron, F. et al. Permanent fore-arc extension and seismic segmentation: Insights from the 2010 Maule earthquake, Chile. *J. Geophys. Res.* **118**, 724–739 (2013).
22. Miyakawa, A. & Otsubo, M. Effect of a change in the state of stress on the likelihood of inland fault failure during the Mw 66 Iwaki earthquake resulting from the Mw 90 Tohoku earthquake, Japan. *Tectonophysics* **661**, 112–140 (2015).
23. Cortés-Aranda, J., González, G., Rémy, D. & Martinod, J. Normal upper plate fault reactivation in Northern Chile and the subduction earthquake cycle: From geological observations and static coulomb failure stress (CFS) change. *Tectonophysics* **639**, 118–131 (2015).
24. Salditch, L. et al. Earthquake supercycles and long-term fault memory. *Tectonophysics* **774**, 228289 (2020).

Acknowledgements

We thank Camilo Rojas and Paulina Rivera for their assistance during the field campaigns and Digital Elevation model preparation. Joaquin Cortes helped us to define trench location and mapping a preliminary version of the trench walls. Additionally, thanks are given to Luciana Noguera, Thays Mineli and Fabiano Pumpim for their assistance during sample preparation and luminescence measurements. This research was supported by the FONDECYT Grant 1200170 (ANID Chile) the FONDAP Grant 1523A0009 (ANID CHILE), and Becas Chile Grant 7422008 (ANID Chile). We would like to thank the reviewers of the manuscript for valuable comments and suggestions.

Author contributions

Conceptualization: GG, LA, Methodology: IA, AS, WA, GG, LA. Investigation: GG, LA, IA, Visualization: GG, LA, Supervision: GG, AS, WA, Writing—original draft: GG, LA, Writing—review & editing: GG, LA, AS.

Declarations

Competing interests

The authors declare no competing interests.

Additional information

Supplementary Information The online version contains supplementary material available at https://doi.org/10.1038/s41598-025-86877-0.

Correspondence and requests for materials should be addressed to G.G.

Reprints and permissions information is available at www.nature.com/reprints.

Publisher's note Springer Nature remains neutral with regard to jurisdictional claims in published maps and institutional affiliations.